University of Padua - Physics and Astronomy Department

Course: Advanced Physics Laboratory.

Academic Year: 2023-24.

Determination of the Muon g-factor through Parity Violation in Cosmic Ray Muon Decay

Andrea De Vita - 2086944 - andrea.devita1@studenti.unipd.it Nicolò Salimbeni - 2090010 - nicolo.salimbeni@studenti.unipd.it

Submission date: 14/05/2024

Contents

1	Intr	roduction	2
2	The	eory	3
	2.1	Cosmic Muons	3
		2.1.1 Muon-Detector Interaction	5
	2.2	Principle of the Experiment	6
3	Exp	perimental Setup	8
	3.1	Overview	8
	3.2	SiPM	9
		3.2.1 Gain	10
		3.2.1.1 Analysis	10
		3.2.2 Dark Counts	12
		3.2.2.1 Analysis	12
		3.2.3 Muon Signal Distribution	14
		3.2.3.1 Analysis	14
	3.3	Arietta G25	15
		3.3.1 Arietta Calibration	15
	3.4	Trigger-Veto Configuration and DAQ Efficiency	16
	3.5	Magnetic Field Map	18
4	Res	ults	20
	4.1	Muon Lifetime	20
		4.1.1 Anomalous Intervals Analysis	20
		4.1.2 Lifetime Estimation	21
		4.1.3 Analysis of Sensitivity to the Contribution of Negative Muons	22
	4.2	g Estimation	23
		4.2.1 Correlated Noise Analysis	23
		4.2.2 g Analysis	25
5	Con	nclusions	27

Chapter 1

Introduction

This laboratory report presents a method for determining the magnetic moment of muons, particles characterized by their point-like structure and carrying a unit electrical charge. Muons exhibit a spin of 1/2 and possess a mass approximately 207 times that of an electron. Notably, they also have a non-zero magnetic moment. One example of successful measurements of this property was performed by Amsler, which exploited standard nuclear physics equipment for the study of muons originated from cosmic rays.[1]

This measurement leverages the observed non-conservation of parity in the muon production and decay, first detected in Garwin's experiment.[4] In particular, as a consequence of parity violation, there is a net polarization of cosmic muons that have been stopped in a material at Earth's surface. By putting this material in a known magnetic field, the spins of the stopped muons precess in the field. The spins of the muons (antimuons) are correlated to the direction of the electrons (positrons) emitted in the decays. By measuring the distribution of electrons (positrons) in a certain direction as a function of time, it is possible to determine the precession frequency of the muons (antimuons) and from this the magnetic moment of the muon.

In chapter 2, it is briefly described the origin of cosmic muons and their properties relevant for this measurement. Moreover it is introduced the principle of the experiment. The experimental setup and measurements are described in chapter 3. Finally, results are then discussed in chapter 4.

Chapter 2

Theory

This chapter discusses the main properties of muons and in particular a general description of cosmic muons. Then the process of interaction between such particles and thin layers of material is presented. Finally, the operating principle of the experiment is described, dwelling on the objective of measuring the g-factor of muons.

2.1 Cosmic Muons

Cosmic muons are produced in the decays of pions and kaons originating from the interactions of primary cosmic rays, predominantly protons and light nuclei, with the Earth's atmosphere. Pion decay yields a significantly higher abundance of cosmic muons compared to kaon decay due to the greater probability of pion creation in the primary interactions. Although the following discussion primarily addresses muons from pion decay, its principles extend to muons originating from kaon decay as well.[2]

Charged pions decay by weak interaction according to

$$\pi^+ \to \mu^+ + \nu_{\mu} \text{ and } \pi^- \to \mu^- + \bar{\nu}_{\mu}$$

In the pion rest frame, decays are isotropic in the full solid angle of 4π . However, since created pions have momenta toward the Earth, determined by the initial directions of primary cosmic rays, most of the produced muons also have momenta directed toward the Earth.[7] On Earth's surface, the mean muon energy is approximately 4 GeV and the total downward-directed flux of muons with energies higher than 1 GeV is approximately 1 cm⁻² min⁻¹. Due to the positive charge of the primary cosmic rays, the ratio of the number of positive-to-negative cosmic muons is about 1.25 in the GeV range.[12]

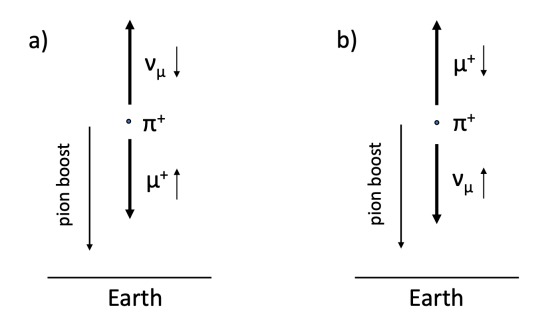


Figure 2.1: Muon production scheme. A positive muon emitted in the pion boost direction in the rest frame of decaying pion (a). A positive muon emitted in the opposite direction of the pion boost in the rest frame of a decaying pion (b).

In pion decay, there is maximal violation of parity and, in the rest frame of a positive pion, the produced antimuon is always left-handed, i.e. its spin is in the opposite direction of its momentum. This property is the consequence of the conservation of the total angular momentum and the fact that pions have spin zero and neutrinos can only be left-handed. On the other hand, since antineutrinos can only be right-handed, negative muons can only be right-handed when produced in the rest frame of the negative pions.[7]

It is caused by parity violation in the processes of pion decay and by the energy spectra of pions from which the muons are produced. To explain this point, let us consider two extreme cases, one in which the muon is emitted in the direction of the pion boost in the rest frame of the decaying pion, i.e. toward Earth's surface (forward muon), and the other in which the muon is emitted in the opposite direction of the pion boost in the rest frame of the decaying pion, i.e. away from Earth's surface (backward muon). If we consider positive pions, in the forward muon case, the μ^+ is emitted toward Earth and the ν_μ is emitted in the opposite direction (see Fig. 2.1a). Thus, forward muons, which are initially left-handed, remain left-handed when they arrive at Earth's surface. In the backward muon case, since it is left-handed the momentum of the produced μ^+ in the rest frame of the decaying pion is in the opposite direction of both the pion boost and its spin (see Fig. 2.1b). Thus positive backward muons that reach Earth's surface (i.e., the muons for which the boosts of the decaying pions were sufficiently large to reverse the initial direction of the backward muons) will be right-handed at Earth's surface.

A complete analysis of all decay angles shows that a net zero polarization can only be due to flat production spectrum. Since the number of pions decreases with the pion energy, an excess number of forward muons will reach Earth's surface, producing a net upward polarization of positive muons at Earth's surface.[7]

The analogous consideration is also valid for negative muons and, keeping in mind that they are produced as right-handed particles, their net polarization at Earth's surface will be downward. The μ^+ polarization has been measured (see Fig. 2.2 on the left) and found different from zero.[1]

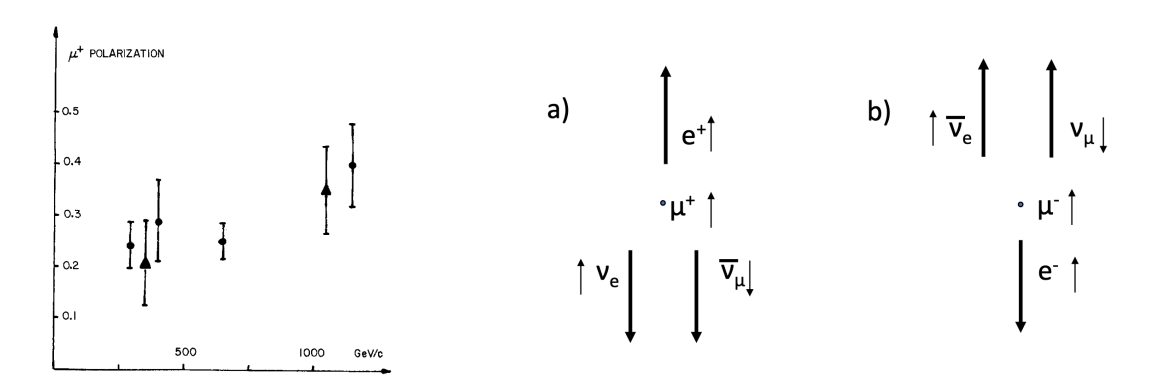


Figure 2.2: On the left. Polarization of μ^+ as a function of momentum at sea level. On the right. Decay at rest of a positive (a) and a negative (b) muon with the emission of the most energetic positron and electron, respectively.

Muons decay via the weak interaction with a mean lifetime of $\tau = 2.1969811 \pm 0.0000022 \ \mu s$. Parity violation is also present in these decay processes, which proceed as follows:

$$\mu^+ \to e^+ + \nu_e + \bar{\nu}_{\mu} \text{ and } \mu^- \to e^- + \bar{\nu}_e + \nu_{\mu}$$

The directions of the emitted positrons (electrons) in these decays are correlated with the above described net polarization of the muons at Earth's surface, producing an asymmetric angular distribution. This fact can be qualitatively understood if, in the decay of a muon at rest, we consider the extreme case where the most energetic positron (electron) is emitted. In this case,

both the neutrino and antineutrino must be emitted in the direction opposite that of the positron (electron), as in figure 2.2 on the right.[1] Since neutrinos and antineutrinos have an opposite handedness, the total angular momentum carried by them is zero, and a positron (electron) must be emitted with the spin parallel to that of the decaying muon. To meet this requirement, and since positrons (electrons) are right-handed (left-handed), their momenta should be directed in (opposite to) the directions of the muon spin. So, for the decays of positive muons, positrons are favorably emitted in the direction of the muon spin, and for the decays of negative muons, electrons are favorably emitted in the opposite direction of the muon spin.[1]

2.1.1 Muon-Detector Interaction

A charged particle penetrating through matter loses its energy in numerous Coulomb collisions at random points along its track. The total energy loss, in a track segment of length s, is a stochastic quantity whose distribution is described in terms of a straggling function, $f(\Delta, s)$.[6] For detectors of moderate thickness s, i.e. one where the ionization losses are significantly smaller than the initial energy of the particles, the energy loss probability distribution is adequately described by the highly-skewed Landau (or Landau-Vavilov):[3][6][11]

$$f_{LV}(\lambda, x) = \frac{1}{\xi(x)} \frac{1}{2\pi i} \int_{a-i\infty}^{a+i\infty} \phi(s) e^{\lambda s} ds, \quad a \in \mathbb{R}$$
 (2.1)

where x is given in $g cm^{-2}$ and

$$\phi(s) = \exp[k(1 + \beta^2 \gamma_E)] \exp[\psi(s)]$$
(2.2)

$$\psi(s) = s \log k + (s + \beta^2 k) \left[\int_0^1 \frac{1 - e^{-st/k}}{t} dt - \gamma_E \right] - k \exp(-s/k)$$
 (2.3)

$$\lambda = \frac{\Delta - \Delta_p}{\xi} \quad \text{with } \xi = 0.300 \frac{m_e^2 Z}{\beta^2 A} \cdot x \tag{2.4}$$

In these equations γ_E is the Euler's constant and k is proportional to the ratio of the mean energy loss over the path length to the largest energy transfer possible in a single collision with an atomic electron. Δ_p is the mode of the Landau distribution.[3]

The underlying significance of this result lies in the fact that the limited thickness of the absorber constrains the number of collisions, preventing the application of the central limit theorem.[6] Consequently, the final distribution can not be described by a gaussian (see Fig. 2.3). Thus, the most probable value for energy loss is not equal to the mean value predicted by the Bethe-Bloch model. This deviation occurs due to the substantial influence of infrequent events involving high-energy transfer, which imparts considerable fluctuations to the mean in an experimental distribution of a few hundred events.[11] Thus it is possible to study energy loss within thin detectors through the most probable value from Landau-Vavilov distribution:

$$\Delta_p = \xi \left[\ln \frac{2mc^2 \beta^2 \gamma^2}{I} + \ln \frac{\xi}{I} + j - \beta^2 - \delta(\beta \gamma) \right]$$
 (2.5)

where $\delta(\beta\gamma)$ is a density correction introduced by Bichsel, I is the mean excitation energy and $j \approx 0.200$ is a negligible constant.[11]

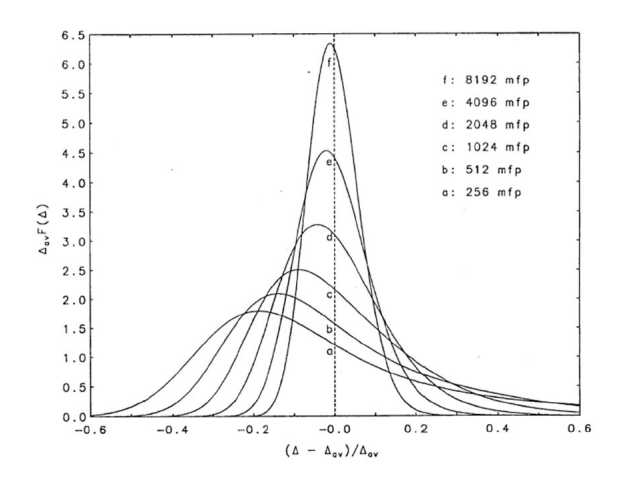


Figure 2.3: Energy loss PDFs are plotted for various thicknesses of water absorbers, where the thickness is expressed in units of mean free path (mfp). For visual clarity, the energy loss PDFs have been scaled on both the abscissa and ordinate. The single event energy loss is expressed as a fraction of the mean energy lost in the entire absorber thickness.[8]

2.2 Principle of the Experiment

A charged particle with a spin carries a magnetic moment. For the muon, which is a point-like lepton, the magnetic moment is given by

$$\vec{\mu}_{\mu} = g_{\mu} \mu_{\mu}^{Bohr} \vec{s} \tag{2.6}$$

where g_{μ} is called g-factor and μ_{μ}^{Bohr} is the Bohr magneton of the muon given by $\mu_{\mu}^{Bohr} = \frac{e\hbar}{2m_{\mu}}$. g_{μ} is predicted by the Dirac equation to be exactly 2 for leptons, but experimentally its value differs slightly from this theoretical expectation.[2]

If a muon is in an external magnetic field B, its spin will precede with the angular frequency

$$\omega = g_{\mu} \frac{eB}{2m_{\mu}c} \tag{2.7}$$

Therefore, if cosmic muons are stopped in a suitable non-magnetic material that is immersed in a horizontal magnetic field (with respect to Earth's surface), there will be a precession of spins of the stopped muons.[1] Copper is one such suitable material because it effectively stops cosmic muons due to its relatively high density and atomic number. Positive muons are stopped in the material and they decay as free particles, while most of the negative muons are quickly caught by nuclei in the stopping material (the lifetime of negative muons in copper is $0.163~\mu s$).[9]

The muon spin precession is determined by detecting positrons from the decays of stopped muons only in the upward direction. [1][2]

In section 2.1 it is explained that the net polarization of the cosmic muons at Earth's surface is not zero, so the precession of their spins in the magnetic field yields oscillation in time of the number of detected positrons from the decays about the usual exponential decay curve.[2]

When there is no magnetic field, the data from the experiment should follow a simple exponential dependence

$$N(t) = C + N_0 e^{-t/\tau} (2.8)$$

where τ is the muon mean lifetime.

With an applied magnetic field, with good accuracy, it is expected the following relation:

$$N(t) = C + N_0 e^{-t/\tau} \left(1 + A \cdot \cos(\omega t + \phi) \right)$$
 (2.9)

where A is the experimental asymmetry¹, ω is the muon precession frequency, and ϕ is the angle of initial muon polarization.[1] By fitting the function 2.9 to the measured time distribution, which is obtained by detecting upward emitted particles from the decays of muons that are stopped in the material in the horizontal magnetic field, it is possible to determine the frequency of the muon precession ω , and hence g_{μ} from equation 2.7.[1][2]

¹This quantity depends on the asymmetry of the positrons emitted in the muon decays, the polarization of the stopped muons, and the geometry of the setup

Chapter 3

Experimental Setup

This chapter discusses the experimental setup and the preliminary study of the performance of the different components. As for the SiPMs, their characterization is expressed in terms of gain and dark counts. The trigger and veto signals are described dwelling on the relationship between the choice of threshold and the efficiency and false-positive values of the acquisition system. In particular, the latter also consists of a chip for measuring the muon decay time: Arietta is studied to define the relationship between the returned values and the corresponding time difference. Finally, a study of the homogeneity of the magnetic field inside the solenoid is presented.

3.1 Overview

The experimental configuration depicted in figure 3.1 comprises two trigger layers situated above an absorber medium, followed by a veto layer. Each trigger and veto layer consists of $60 \times 25 \times 1$ cm³ EJ-200 plastic scintillator plates with embedded optical fibers, while the absorber is a copper plate with an effective volume of approximately $60 \times 25 \times 2$ cm³. The scintillating optical fibers consist of a polystyrene-based core (n=1.60) and a PMMA cladding (n=1.49) and they are blue-to-green wavelength shifters. The setup is contained within a copper solenoid measuring $\approx 92 \times 60 \times 12$ cm³, producing a magnetic field of approximately 5.6 mT at its center with a current of 5 A.

Regarding front-end electronics, the scintillator signals are captured using a pair of SiPMs for each layer: thereafter the individual SiPMs of the pairs will be denoted by L (left) and R (right). The digital conversion and trigger-veto logic are handled by a CAEN VME module with an integrated ADC. The resulting digital signal is utilized by an Arietta G25 to record the time gap between successive events, indicating the absorption of a muon (antimuon) and the emission of an electron (positron), thus enabling the determination of the muon lifetime. For a comprehensive understanding of the trigger-veto logic, refer to section 3.4. Additionally, the technical specifications of the Arietta chip are detailed in section 3.3.

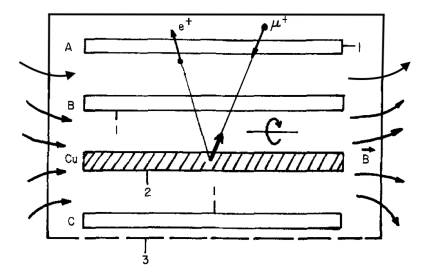


Figure 3.1: Experimental setup overview. 1-plastic scintillator (A,B and C). 2-copper target. 3-coil.

3.2 SiPM

The silicon photomultiplier (SiPM) is a radiation detector with extremely high sensitivity, high efficiency, and very low time jitter.[5] It is based on reversed biased pn junction and it can directly detect light from near ultraviolet to near infrared. SiPMs are employed in all those applications where low light/radiation levels must be measured and quantified with high precision.[5]

A SiPM consists of a matrix of small-sized sensitive elements called micro-cells (or pixels) all connected in parallel. Each micro-cell is a Geiger-Mode avalanche photo-diode (GM-APD) working beyond the breakdown voltage (V_{br}) and it integrates a resistor for passive quenching.[5] In quiescent mode, the diode is reversed biased to $V_{bias} = V_{br} + V_{ov}$ (V_{ov} is the overvoltage, i.e. the excess bias beyond V_{br}) and no current flows through the circuit.[5]

Once triggered, the avalanche process is self-sustaining meaning that a steady current flows indefinitely in the device. In order to avoid this effect, each pixel has a quenching resistor R_q which helps in reducing inverse polarization and therefore it is useful to stop avalanche effect. In addition, R_q decouples each pixel from the others, allowing them to operate independently despite common power supply (see Fig. 3.2).[5]

There are two main working phases: discharge phase and recovery phase. The first one corresponds to the rising edge of the signal (time constant $C_J \cdot R_s$, with R_s as the internal diode resistor), while the slower trailing edge is the recovery phase with time constant $C_J \cdot R_q$. The amplitude of the SiPM pulse increases with the overvoltage while both the rising time and the recovery time are mainly determined by C_J , R_s , and R_q .[5]

During recovery, the GM-APD cannot detect other photons. For this reason, a GM-APD cannot count the number of incoming photons unless the photon rate is lower than the inverse of the recharge time. SiPMs overcome this limitation thanks to the parallel arrangement of several micro-cells. When N photons are detected (which means that N photons arrive on N different micro-cells producing N single-cell signals) the SiPM output pulse is N-times larger than the single-cell response.[5]¹

Note that both the amplitude and the area of each SiPM pulse, which is the total charge delivered by the detector, are proportional to the number of detected photons (neglecting primary and correlated noise for the time being). If the number of incoming photons is larger than the number of micro-cells in the SiPM, saturation occurs and neither the amplitude nor the area of the output pulse can give information on the number of incoming photons anymore.[5]

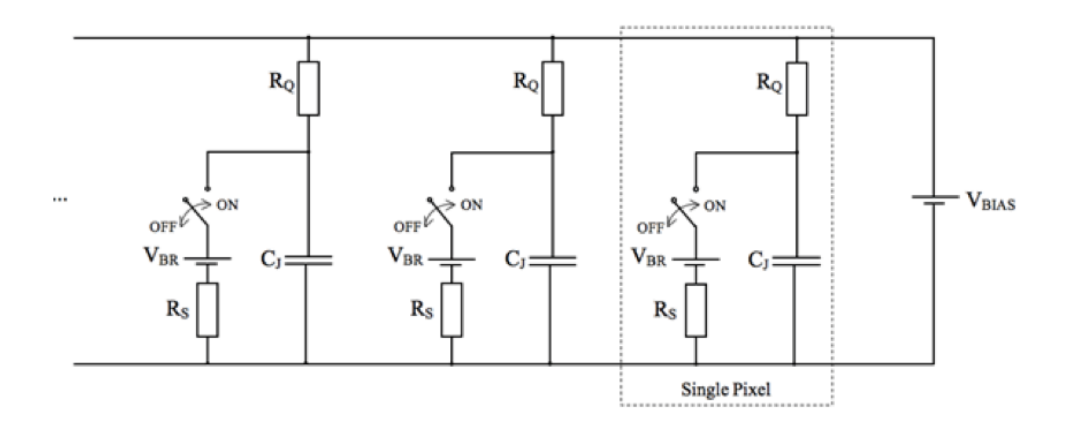


Figure 3.2: Equivalent circuit of a SiPM. The dashed rectangle outlines a single pixel.

¹For the sake of clarity, employed SiPMs return negative amplitude signals, but the analysis treated them as unsigned values. For this reason some histograms contain positive values.

3.2.1Gain

The gain for SiPM is defined as the ratio of the charge produced by the detector to the primary charge that generated the avalanche. In particular, the latter corresponds to the elemental charge of the electron, since SiPMs are single-photon devices, which generates at most one electron-hole pair. [5] Thus the expression of the gain is the following

$$G = \frac{Q}{q} = \frac{Q}{e} \tag{3.1}$$

In order to study the trend of gain in relation to the experimental setup, it is necessary to describe the quantity at the numerator. [5] The total charge produced is defined as the integral of the current signal. So in order to be able to estimate this quantity, it is necessary to describe the operating steps of the detector:

- 1. ready state: the voltage (V_D) at the ends of the photodiode is equal to V_{bias} . The equivalent circuit switch is open and, as long as a photon is not absorbed, the device remains in this condition in which current does not flow (see Fig. 3.3).[5]
- 2. **triggered state**: when a photon is absorbed and the avalanche is triggered, the switch instantaneously closes and the C_J begins to discharge across the R_s resistor. Thus the detector is in the discharge phase.[5] The voltage at the ends of the capacitance decreases to $V_{min} = V_{bias} - \frac{R_q(V_{bias} - V_{br})}{R_s + R_q}$ and then the avalanche stops and the switch opens (see Fig. 3.3).[5]
- 3. recovery phase: C_J recharges through R_q to V_{bias} and the detector returns to its initial state, ready for the detection of another photon (see Fig. 3.3).

When the cell is in the ready state, the current i(t) is negligible. However, upon triggering avalanche, the current rises following the function

$$i(t) = i_{\text{max}} \left[1 - e^{-t/(R_s C_J)} \right]$$
 (3.2)

where i_{max} is determined by $i_{\text{max}} = \frac{(V_{\text{bias}} - V_{\text{br}})}{R_q}$.[5] Subsequently, a recovery phase occurs, during which V_D is restored to V_{bias} , accompanied by a declining current described by

$$i(t) = i_{\text{max}} \cdot e^{-t/(R_q C_J)}. \tag{3.3}$$

Upon integrating from t_i to infinity, it becomes that $Q = C_J(V_{\text{bias}} - V_{\text{br}})$.[5] As a result, the final expression for the gain can be presented as follows:

$$G = \frac{C_J(V_{\text{bias}} - V_{\text{br}})}{q} \propto V_{\text{bias}}$$
(3.4)

3.2.1.1Analysis

The objective of this study is to evaluate the best operating region for each of the 6 SiPMs available (A-R is broken, thus the actual number of devices is 5).

In order to be able to evaluate the gain as a function of bias voltage, it is necessary to redefine it in terms of the physical quantities being analysed: looking at the figure 3.4 on the left, it can be seen that the spectrum of voltage signal maxima produced by the SiPM is not continuous, but it has peaks at regular intervals. These peaks correspond to the signals generated by the production of n electron-hole pairs. Therefore, by studying the voltage distance between the maxima of the peaks in the histogram, it is possible to evaluate the gain in terms of voltage

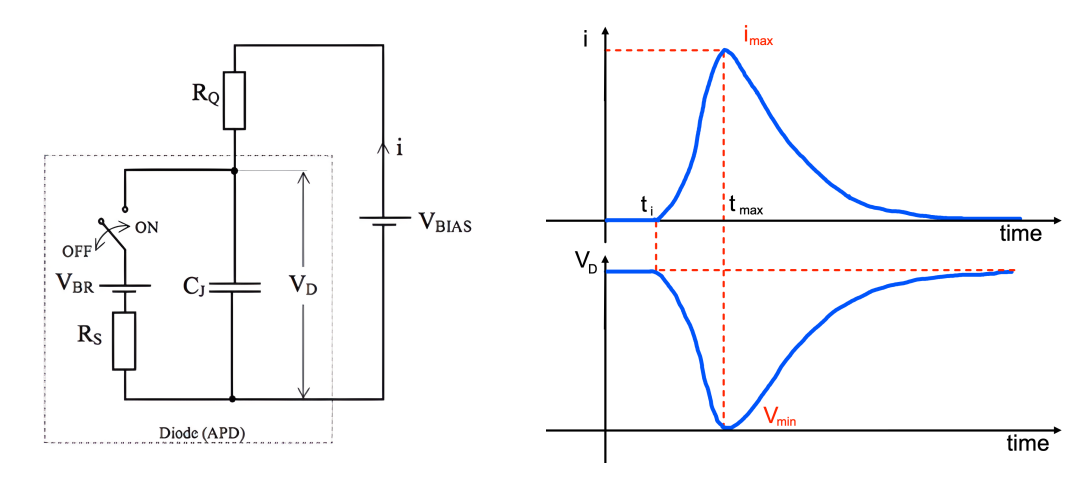


Figure 3.3: On the left. Equivalent circuit of a SiPM cell externally supplied with V_{bias} . The switch is in the OFF position when the APD is in the charging phase; while it is ON at the time when charging triggers an avalanche. On the right. Current pulse generated in a cell during avalanche and the corresponding change in voltage at the ends of the junction (V_D) .

signal produced by a single e-h pair. With respect to the conducted study, gain is thus defined as voltage signal per number of pairs.

This definition allows this quantity to be estimated by averaging the distance between peaks, thus expressing the gain in mV or mV/pair. In this way, it is possible to interpret the voltage at null signal as the breakdown voltage V_{br} .

As anticipated, the histogram shown in figure 3.4 on the left represents the spectrum of the voltage signal maxima produced by a SiPM. The configuration adopted for signal sampling used a trigger threshold of -4 mV to eliminate fluctuations not related to real events, while the time window considered was 200 ns before the trigger and 500 ns after it to account for the slow charge phase of the junction.

Once the trigger is configured, it is possible to reconstruct the spectrum of the signal maxima for different values of the bias voltage. For each of these, the mean value of the distances between the peaks is evaluated, then for each SiPM a set of

SiPM	V_{br} [dV]
A-L	282 ± 9
B-L	290 ± 20
B-R	280 ± 20
C-L	280 ± 7
C-R	280 ± 20

Table 3.1: V_{br} values from the fit performed for each SiPM.

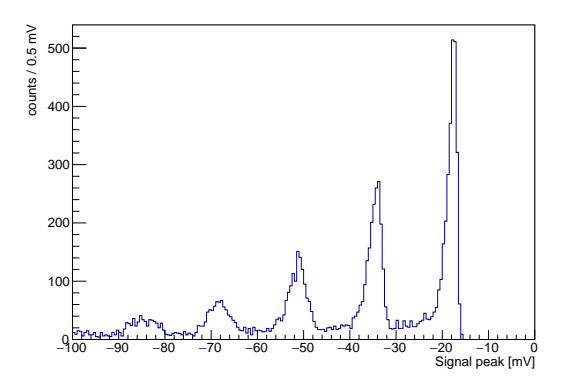
values for bias voltage and gain with relative errors is obtained. In particular, the uncertainty on the bias voltage was set at 3 dV, taking into account the resolution of the voltage generator (1 dV) and some random errors, which are related to fluctuations in the value of the voltage due to thermal in the internal circuit of the generator. As far as the gain uncertainty is concerned, it is evaluated using the following formula:

$$\sigma_G = \sqrt{\frac{\sum_{i=1}^N \left(G - \overline{G}\right)^2}{(N-1)N}} \tag{3.5}$$

It is now possible to fit the collected data with the function $G = a \cdot V_{bias} + b$, from which it is possible to extract the value of V_{br} as the intercept to the x-axis

$$V_{br} = \frac{-b}{a} \tag{3.6}$$

The results of the analysis conducted on SiPM A-L are shown in figure 3.4 on the right, while table 3.1 contains the overall results of the fit for each of the available SiPM.



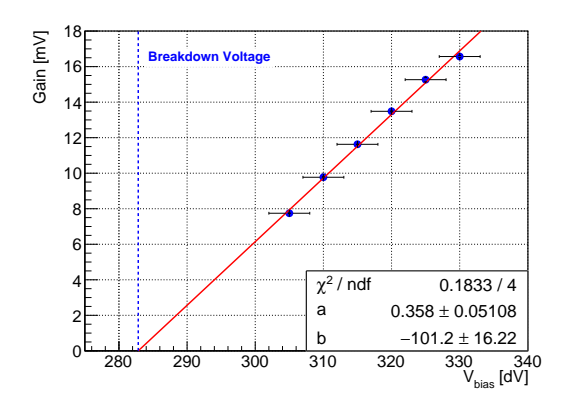


Figure 3.4: On the left. SiPM A-L spectrum of signal maxima operating with a bias voltage of 330 dV. On the right. Results of gain fit at varying bias voltage for SiPM A-L. The red line represents the linear fit, while the blue dashed line intercepts the breakdown voltage.

3.2.2 Dark Counts

At room temperature silicon detectors are subject to dark counts due to thermal excitation. Due to heat, some electrons can jump from the valence band to the conduction band, so if they are produced within the depletion region, they are accelerated by the electric field, leading to an avalanche.[5] This thermal effect causes the production of signals that contribute to the so called dark counts and the main goal of this analysis is to study how dark counts vary as a function of the applied potential. The triggering efficiency, i.e. the probability for a charge carrier to generate an avalanche by ionization, increases with the overvoltage till a saturation value is achieved. As a consequence, it is expected that the number of dark count events increases with V_{ov} .[5]

Therefore, it is sufficient to construct a graph (bias voltage, noise counts rate) which will intersect the x axis at a certain value. This is precisely the value at which avalanches begin to be observed: by definition it is the breakdown voltage.[5]

To perform this analysis the sensors were connected directly to the oscilloscope and a threshold lower than the height of the single photon signal was applied. At this point, being able to also keep track of the data taking time, the dark count rate is the following:

$$dark counts rate = \frac{number of counts}{time to acquire those counts}$$
 (3.7)

Unfortunately, due to non-negligible noise, the number of counts was very high, leading to barely indistinguishable peaks. It follows a full discussion of the acquisition and analysis of dark counts.

3.2.2.1 Analysis

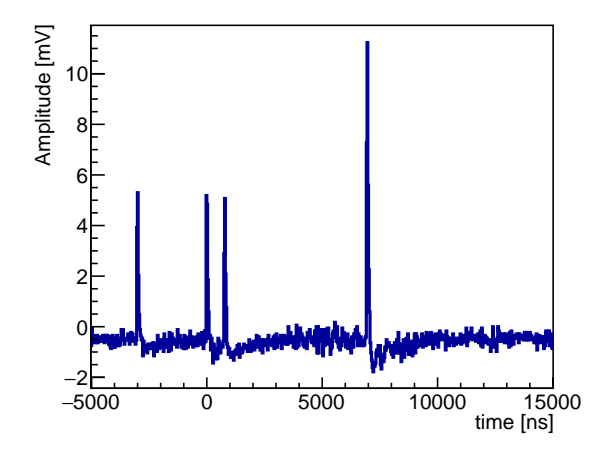
The acquisition system works using a trigger, when a signal exceeds a certain threshold a trigger is launched and a histogram (see figure 3.5) with a certain portion of the signal is saved in a root file.

The problem is that the time window that covers each single histogram (trigger) is relevant to the analysis and it can be understood by making an extreme case. Let us imagine a very short time window, so for each trigger only the signal that launched the trigger itself is saved in the histogram. This will lead to a constant noise count as each measure counts only one event:

$$\frac{\text{number of triggers} \times 1}{\text{number of triggers} \times \text{time with of the histogram}} = \frac{1}{\text{time with of the histogram}}$$
(3.8)

which has nothing to do with the sensors but only with how the data was acquired.

To solve the problem, it is sufficient to greatly widen the time window acquired per trigger so



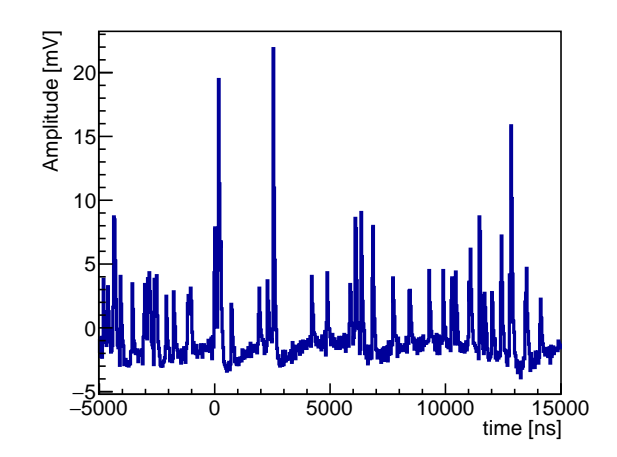


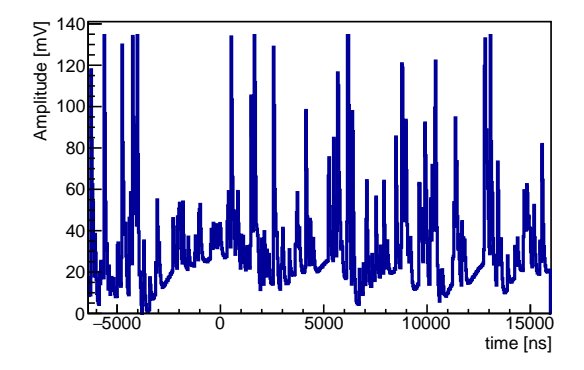
Figure 3.5: Example of what is acquired every time the data acquisition system receives a trigger for a not noisy SiPM (on the left) and for a noisy SiPM (on the right).

as to make the fact that there will always be at least one signal in the histogram (the one that launched the trigger) essentially negligible.

Let us now address the issue of data analysis. The signal obtained is not necessarily composed of well-defined peaks interspersed with areas of zero signal. It is possible that there is background electronic noise that generates small unwanted peaks, usually smaller than those of a single photon. An example is shown in figure 3.5 on the right.

For this reason, it was exploited a smoothing algorithm proposed by Silagadze, ending up with and histogram like in figure 3.6 and then looking for the peaks by hand in the smooth histogram.[10]

The algorithm sometimes fails and hides low peaks, or if two are too close they are merged into one. Thus, it is necessary to make attempts and modifying the input parameters in order to minimize this effect.



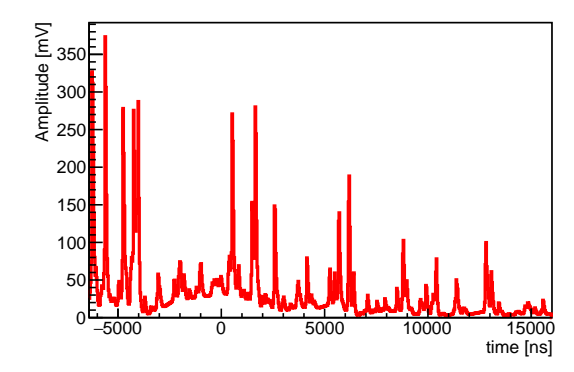


Figure 3.6: On the left. Example of what is acquired every trigger for noisy SiPM. On the right. Smoothed version using the method proposed by Silagadze.[10]

Regarding uncertainties, they were estimated by combining in quadrature two main sources: the Poissonian contribution from the number of counts and the error introduced by the smoothing algorithm. The latter was calculated as follows. The only parameter, called n, relevant for histogram smoothing is on how many bins to "average", a value has first been decided using graphs like those shown in figures 3.5 and 3.6. Then n was increased and decreased by one, obtaining two more estimates of the dark counts, one with more counts, but noisier, one with fewer counts, but in which some events are merged. A uniform distribution was then applied to

these two extreme values, obtaining an estimate of the algorithm's error.

In conclusion, below in figure 3.7 there are the values obtained for the rate of dark counts per μs for SiPM B-R and C-R (respectively a noisy and not noisy one) as a function of the applied bias.

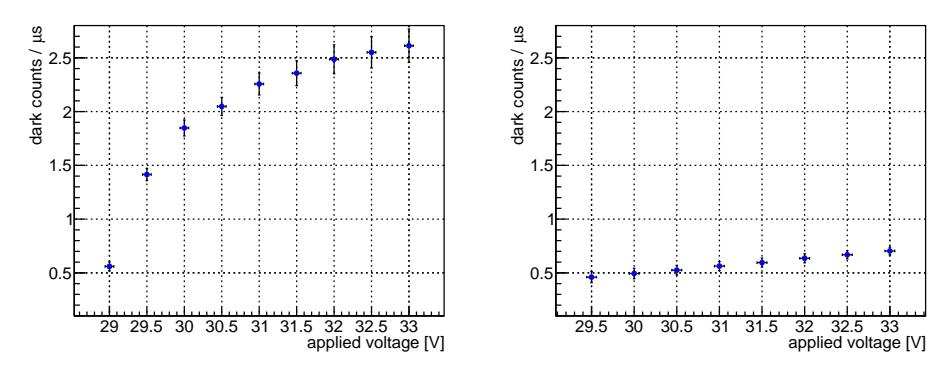


Figure 3.7: Dark counts rate as a function of the bias for SiPM B-R on the left (noisy), and SiPM C-R on the right (not noisy). They are plotted on the same y-range for a better comparison.

3.2.3 Muon Signal Distribution

Assuming that the number of produced photoelectrons, and consequently, the signal, exhibits a linear relationship with the energy that is released, the distribution of signal peaks conforms to eqn.2.1 distribution with $x \to -x$ because voltage signals typically have negative amplitudes.

3.2.3.1 Analysis

To confirm the adherence of signal distributions resulting from muon interactions to the Landau-Vavilov distribution model, a trigger threshold of -75 mV was used so that events resulting from noise and muon interactions could be distinguished.

This choice is grounded in the assumption that these interacting muons are of atmospheric origin, hence with enough energy to generate signals with significant amplitudes in contrast to the typical voltage induced by noise and less energetic particles. Moreover it is important to note that this analysis does not require the sampling of every single muon; the exclusion of certain events is acceptable and does not preclude a successful analysis.

The trigger relied on the logical coincidence of the digitized signals from the external SiPMs. This approach allowed us to trigger events corresponding to muons that traversed all three scintillator layers, enabling us to investigate the energy deposition within the inner layer. Specifically, we focused on analyzing the signal from one of the SiPMs within that layer.

\mathbf{SiPM}	$\Delta_p [\text{mV}]$
A-L	-63.21 ± 0.05
B-L	-58.34 ± 0.07
B-R	-56 ± 1
C-L	-70 ± 3
C-R	-77 ± 2

Table 3.2: Most probable values for each SiPM from the fit with a Landau-Vavilov distribution.

Excluding the small noise peak near the origin, the shape of this distribution qualitatively resembles a Landau-Vavilov distribution (see Fig. 3.8).

An important parameter of this distribution is the most probable value of the energy energy loss. As described in section 2.1.1, this holds significance for future analyses as it provides an estimate of the order of magnitude for signal amplitudes. This information aids in determining the appropriate trigger threshold for distinguishing genuine events from noise, striking a balance between discrimination and number of sampled events (see Sec. 3.4). The results of this analysis are shown in table 3.2.

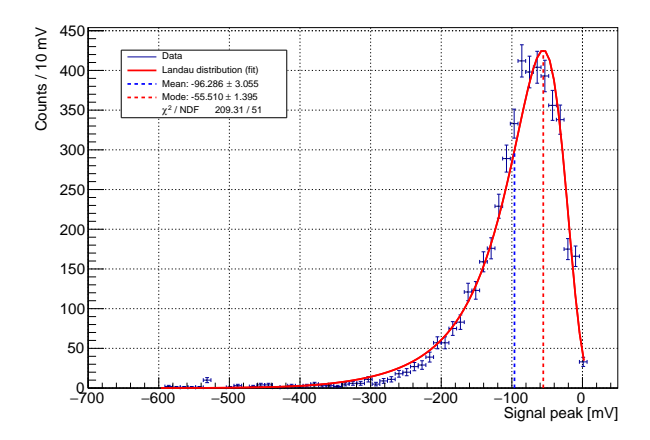


Figure 3.8: Signal distribution of SiPM B-R with the MPV and mean values underlined by two vertical dashed lines.

3.3 Arietta G25

Arietta G25 is a GNU/Linux embedded microcomputer based on a 400 MHz ARM9 processor. Its usage in the acquisition system involves analyzing incoming NIM signals to measure the time interval between two subsequent signals. The following section outlines the calibration of this component of the experimental setup, particularly to characterize Arietta in terms of the shortest measurable Δt and the minimum duration of the input signals.

3.3.1 Arietta Calibration

As mentioned before, Arietta expects two input signals a short distance from each other. When the first signal arrives it starts counting clock cycles. If another signal arrives within a certain time window from the first one then this is interpreted as a stop, and the number of clock cycles is written into a register. This procedure depends on various system variables. The main ones, which have been studied or taken into consideration, are the following: the shape of the signals, the duration of the signals, the distance between one signal and another.

First it is good to explain how the test signals were sent to Arietta. By using the oscilloscope, it is possible to generate two square waves at variable distances from each other. Then instead of sending these pulses directly to the board they were first sent to the digital electronics to mimic the real coincidence signal from the complete setup. The output signal was then sent to the board to get the start and stop signals. This was done so as to calibrate Arietta with signals of the same shape as the signals it will then receive during data analysis.

The first to address is the shape of the signal. The signal shape dependence of Arietta G25 efficiency is related to the fact that it is necessary to provide the board with signals that can be easily converted to make them compatible with the needs of the board. Irregular input signals could lead to incorrect conversion and consequently to worse performance in measuring time differences. Since the start and stop signals come from the digital electronics they are of a well-defined shape. These signals, due to the precision at which the measurements are made, can be considered almost perfect square waves, consequently the only variable to take into consideration is their duration. If a signal is too short it risks not being received, resulting in missing events. To study Arietta efficiency as a function of the duration of the signals, two signals were sent spaced from each other of a time interval of 1 μ s, at a frequency of 100 kHz (every 10 μ s). This Δ t was chosen as it is a quantity comparable to the average lifetime of the muon, which is what we want to measure. Results are reported in table 3.3 and it can be noticed that below a certain duration Arietta no longer sees anything.

Width [ns]	Efficiency
135	1
92	0.995
80	0.995
69	0.998
52	0.999
49	0.9985
45	0

Table 3.3: Arietta efficiency on signal detection as a function of signal width, the distance between two signals is fixed at 1 μ s.

$\Delta t [ns]$	Efficiency
190	0.999
139	0.999
89	0.9985
80	0.9985
78	0

Table 3.4: Arietta efficiency on signal detection as a function of the distance between the two signals, the width of a signal is fixed at 85 ns.

At this point it is possible to study the efficiency as a function of the distance between two signals. If two of these are too close temporally, they could be mistaken for one, resulting in an undetected event. To carry out this test, the duration of the signals was set to 85 ns, sending them in pairs as previously every 10 μ s. The results are reported in the table 3.4: Arietta has excellent efficiency up to a certain threshold, below which it no longer sees anything.

Finally, it is possible to carry out a temporal calibration. Since the process is linear, it will be sufficient to do a linear fit of the points and then use the result to convert the obtained values. In order to obtain the data points, multiple sets of signal pairs were transmitted in batches of 300, allowing Arietta to record them in its internal register. From these sets, the mean value and the mean error were computed. Consequently, each point on the graph represents the mean values along with the time distance between the signals, a parameter predetermined using the oscilloscope. The calibration results are presented in figure 3.9.

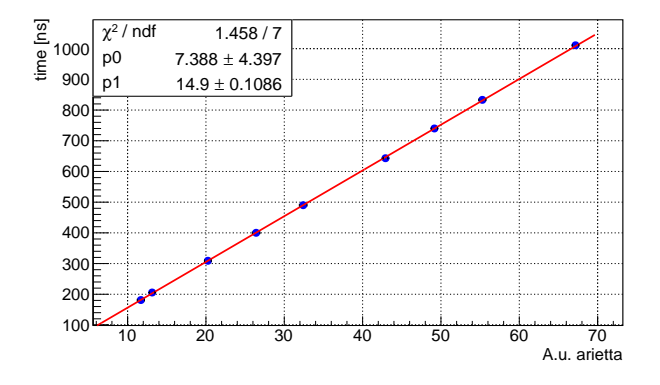


Figure 3.9: Calibration of Arietta using a linear fit. The x-axis represents the output of the card, while the y-axis represents the time interval between the start and stop signals.

3.4 Trigger-Veto Configuration and DAQ Efficiency

As described before, the signals from the three layers of scintillators are digitized on the electronics board through an ADC (see Fig. 3.10 on the left). This process has been configured to produce 3V digital signals. Once the analog signal overshoots a threshold, whose value will be discussed later, a signal is produced with a delay equal to the sum of two contributions: the intrinsic latency of the electronics and a delay configured by the user. Similarly, the duration of the signal is also configured ad hoc (see Tab. 3.5).

The reason for defining the duration and delay of the signals is to ensure that the veto signal

SiPM	Threshold [mV]	Delay [ns]	Width [ns]
A-L	-45	117.5	83.06
B-L	-65	117.5	83.06
B-R	-65	117.5	83.06
C-L	-50	97.5	192.5
C-R	-50	97.5	192.5

Table 3.5: ADC configuration for each SiPM that has been employed.

is generated before the trigger with a duration sufficient to fully cover the latter. The trigger is defined as the coincidence of the SiPM signals above the copper layer, as follows:

$$trig = A_L \wedge B_L \wedge B_R$$

The veto, instead, coincides with the logical AND of the layers below the absorber:

$$veto = C_L \wedge C_R$$

Therefore, configurations must respect these definitions. The width of the individual signals must ensure a minimum width of the coincidences, so that two criteria are met: the first concerns Arietta and it requires that sufficiently wide input signals be generated (see Sec. 3.3.1); the second concerns the veto, which is required to be wider than the trigger signal. Consequently, to ensure a minimum amplitude of signal coincidences, it is necessary to identify the minimum signal amplitude that Arietta can handle and also consider jitter to determine a minimum width of the individual signals contributing to the coincidence: $\tau > \tau_A + \tau_{jitter}$, where $\tau_{jitter} \approx 20$ ns is the digital jitter due to the ADC and τ_A is the minimum width that is seen by Arietta. In the figure 3.10 on the right, it is reported the jitter measurement procedure for the digital signal produced by the analog signal of the SiPM C-L. For veto signals, it is also necessary to take into account the width of the trigger signal to ensure that wider signals are produced ($\tau_{veto} > \tau_{trio}$).

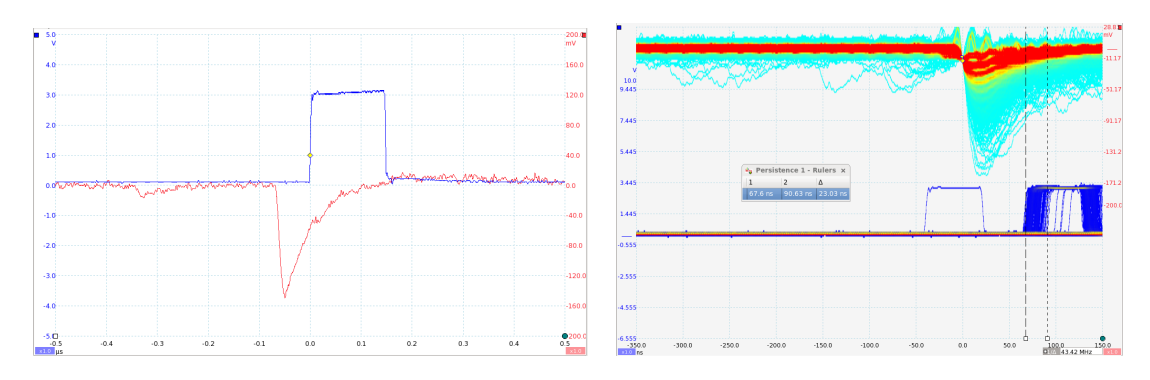


Figure 3.10: On the left. C-L analog signal compared with its digital signal. On the right. Time jitter analysis of the digital signal from the analog signal of SiPM C-L.

This configuration is used to discriminate between particles that completely pass through the apparatus and those that are absorbed in the copper plate. It also allows tagging of particles emitted in the upper hemisphere following the decay of absorbed muons. As a result, the digital signal produced by the electronic board can be defined as follows:

$$sig = trig \wedge \overline{veto}$$

The use of redundant systems limits the number of false positives caused by the dark current of the SiPMs to random or correlated coincidences. In particular, given two SiPMs, the first has a frequency that can be defined by the following expression:

$$f_{12} = (\tau_1 + \tau_2)f_1f_2 \tag{3.9}$$

where τ_i is the duration of the signal ($\approx 100 \ ns$) and f_i is the dark counts frequency.

In table 3.6, it is observed that this value depends on the threshold used by the ADC. Therefore, one can consider the choice of the threshold as a compromise between the number of random coincidences and the efficiency of the apparatus. Increasing this value, in fact, reduces the acceptance frequency of true events. By observing the distribution of signals released in the individual layers of scintillators, it is possible to estimate the efficiency as the integral of the left tail of the threshold. Table 3.6 reports the efficiency values as a function of the threshold. It is noteworthy that the efficiency can be maintained above 75% using the threshold configuration described in the table 3.5. Moreover, these thresholds ensure negligible random coincidence probability for both trigger and veto signals.

	Efficiency [%]				f_{coinc}	[Hz]	
Threshold [mV]	A_L	B_L	B_R	C_L	C_R	Trig.	Veto
-10	96.78	98.68	99.65	99.98	98.76	$2.11 \cdot 10^5$	$1.6 \cdot 10^4$
-50	83.89	80.57	76.97	81.74	85.76	0.16	$4 \cdot 10^{-5}$
-80	61.08	57.20	53.49	65.77	69.77	$1.28 \cdot 10^{-9}$	$3 \cdot 10^{-7}$

Table 3.6: SiPM efficiency and random coincidence frequency of trigger and veto signals as a function of ADC threshold.

3.5 Magnetic Field Map

In this section it is reported the charaterization of the magnetic field produced by the solenoid. It plays a crucial role in this experimental setup and requires careful consideration. As the precession frequency of muons depends on \vec{B} , it's essential to ensure its homogeneity to make the precession speeds uniform for all muons. Any variations in angular velocities would significantly complicate the fit process for estimating q.

To account for all external factors, the magnetic field was mapped using a Hall probe. This probe was placed at different positions within the solenoid to create a 3D map. The probe is capable of measuring only one component of the magnetic field at any given time, here only the results for the z component is presented since it's by far the highest component in the solenoid. It's important to note that the measurement system used for positioning within the solenoid and measuring the magnetic field is not highly precise. It relies on an ultrasonic sensor, which is not ideal for use in the confined space inside the solenoid.

The sensor emits sound waves, which bounce off objects and return, allowing for distance estimation with millimeter-level resolution. Ideally, the sound waves should bounce off the Hall probe to measure its position, but sometimes they bounced off the cavity walls, leading to distorted readings. It is noteworthy that instances of obviously inaccurate results generated by the system were corrected. However, for measurements deemed accurate, no additional investigation was pursued to confirm their precision.

The 3D map obtained for the B_z component of the magnetic field is shown in figure 3.11. Firstly, the graph lacks exact symmetry along the z-axis, indicating a non-uniform density of spires along the solenoid. Consequently, the magnetic field deviates from the expected uniformity. However, it is still nearly homogeneous in the central region, within an acceptable margin of error.

Since the magnetic field is not constant, it is inappropriate to utilize a single value to estimate g from ω . Muons stopping along the copper plates encounter varying magnetic field strengths, leading to different precession frequencies. While this complexity could complicate the analysis,

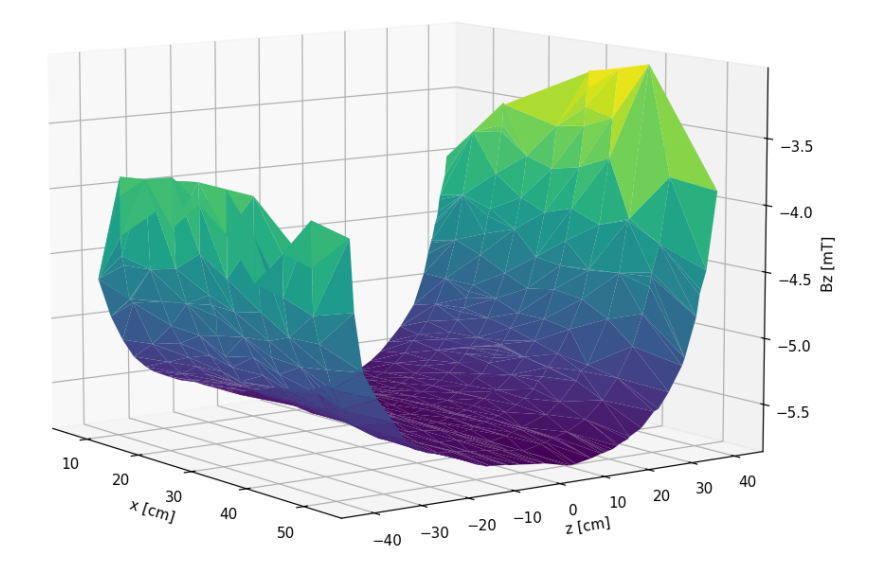


Figure 3.11: Map of the z component of the magnetic field made with the hall probe. Measurements collected at the same y on which the copper was positioned to block the muons.

it falls somewhat beyond the scope of this report. To address this challenge, both physical and data analysis countermeasures were employed.

Physically, the scintillators used are shorter than the solenoid, positioned approximately 15 cm away from the solenoid entrance, where the magnetic field undergoes significant changes. At the analysis level, a single B_z value was employed by averaging the measurements taken within the central 60 cm region where the scintillators are located. The standard deviation of these measurements was used as the error. Despite the significant approximation involved, this approach allows for the estimation of g using a single value, albeit with a notable margin of error:

$$|\vec{B_z}| = (5.6 \pm 0.1) \ mT$$
 (3.10)

This result confirms magnetic field non-homogeneity, which can be estimated at 2%. This phenomenon may arise from external factors, such as the manufacturing process of the solenoid itself, the Earth's magnetic field, the magnetic fields generated by electronic devices surrounding the solenoid.

Chapter 4

Results

This chapter presents the results of the analysis performed with the experimental apparatus studied in the chapter 3. The first analysis concerns the measurement of the average lifetime of the muon, dwelling also on the description of the background present in the collected data. This is followed by the results of the estimation of the muon g-factor. A study of the noise is also presented in this last case.

4.1 Muon Lifetime

In this section, it is described the estimation of the average life of muons by considering several crucial factors. These include the strengths and weaknesses of the experimental apparatus, the identification of background events, and the distinction between positive and negative muons. While the experimental setup has been sufficiently characterized in chapter 3, the focus now shifts to addressing how to incorporate background events (see Sec. 4.1.2) and how to account for negative muons (see Sec. 4.1.3). Before proceeding with these steps, it is crucial to verify whether all events belong to the same distribution. If not, a decision on how to address this issue must be made, this challenge is addressed in the section 4.1.1.

4.1.1 Anomalous Intervals Analysis

In order to study anomalous intervals along the time decay axis, a study of the model function is performed in different time intervals. The idea behind this type of analysis is that the decay times have to be all distributed as a negative exponential with constant background, thus the lifetime parameter has to be independent from the time region of the fit. Figure 4.1 shows that disjoint interval fits are compatible with the fit over the entire range of values, but only fits that ignore the first part of the distribution are compatible with the theoretical value. Firstly, looking at the result of the fit on the right tail, it shows that the standard deviation is larger than in the other intervals, and this can be explain by the fact that fit algorithms converge to a function that is not exponential-like in that region, but it is constant. Thus time decay parameter is not reliable because it is strongly correlated with the exponential normalization. With high normalization constants, lifetime is extremely small, meaning that its contribute is negligible, while, on the other hand, small normalization allows a various range of values for the lifetime parameters.

Additionally, this analysis suggests that the left region leads to high lifetime estimation. This result can be explained by a not constant contribution of noise due to leakage current in the SiPM devices. This causes an increasing frequency of noise events, which occur within the acquisition system as events with short decay times.

In conclusion, the results of this analysis suggests that future analyses will need special caution

with respect to short-time events. In this regard, further fits will ignore the problematic region by limiting the operative range to 2000 ns onward.

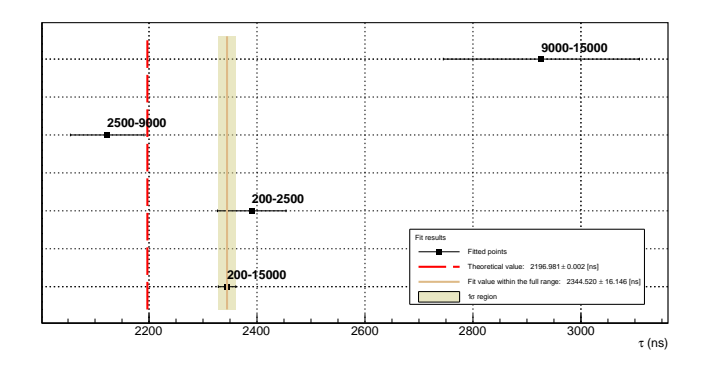


Figure 4.1: τ_{μ} fit within disjoint time intervals compared with a fit within the whole range and the theoretical value (red line).

4.1.2 Lifetime Estimation

In this section it is reported the analysis of muon lifetime based on the muon decay time distribution obtained without a magnetic field. For the moment, this estimation relies on the assumption that the contribution from negative muons is negligible. Further investigations regarding negative muons are detailed in section 4.1.3.

Before proceeding with the comprehensive fit of the data two essential steps must be taken: selecting the fitting range in time and choosing a background model. The analysis conducted in the preceding section revealed a discrepancy between the initial and final points of the graph. To mitigate this issue in the fit, a range starting from 2000 ns onwards was chosen.

Regarding the background, a constant model was adopted. The underlying assumption is that there are no other significantly impactful processes triggering the acquisition system. Consequently, the majority of the background is expected to originate from SiPM noise, occasionally sending pairs of muon-like signals to Arietta.

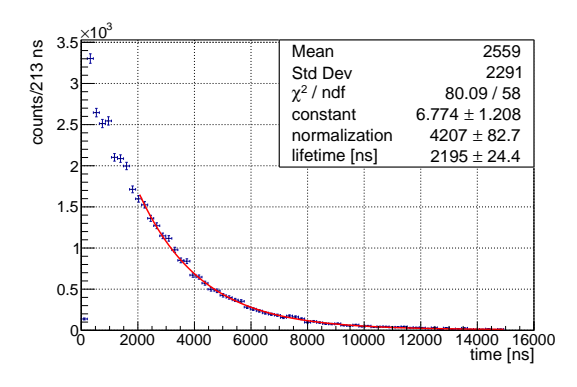
Consequently the function used to perform the fit is (see Fig. 4.2 on the left):

$$f(t) = c + N \cdot e^{-\frac{t}{\tau}} \tag{4.1}$$

It's important to highlight that the constant representing the background is significantly smaller in magnitude compared to the normalization constant of the exponential term. This observation allows to conclude that the background is virtually negligible. This outcome was anticipated, given that an event is identified by the occurrence of two consecutive triggers within a specific time interval. Each trigger involves the coincidence of 5 sensors, making random coincidence highly improbable. The fit algorithm provides an estimation of the average lifetime of the muon:

$$\tau = (2.195 \pm 0.024) \ \mu s$$

However, it's crucial to note that this estimate is highly influenced by the correlation between the parameters τ and N. To facilitate a clear interpretation of this correlation, a colormap of the χ^2 as a function of τ and the normalization parameter N has been generated (see Fig. 4.2 on the right). In examining that graph, there is no attempt to visually identify the minimum; the fit algorithm handles this task. Despite revealing a distinct anti-correlation between the two parameters, it exhibits a single minimum (ideally global), adding credibility to the results.



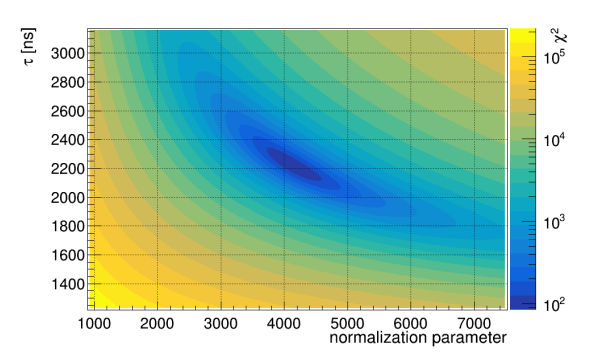


Figure 4.2: On the left. Fit to find moun lifetime using function 4.1. On the right. χ^2 as a function of normalization and τ parameters.

4.1.3 Analysis of Sensitivity to the Contribution of Negative Muons

Another possible study on the collected data is an analysis taking into account negative muons. The objective of this analysis is to investigate the initial segment of the histogram, aiming to establish evidence for an additional contribution to the exponential decay, attributed to the decay rate of negative muons absorbed in muonic states. This process modifies the muon lifetime as the average value is lower than the free particle. As a consequence, a complete model of the collected data is a function that takes into account the antimuons exponential decay, the muon exponential decay and a constant background.

$$f(t) = c + N_{-}e^{-\frac{t}{\tau_{-}}} + N_{+}e^{-\frac{t}{\tau_{+}}}$$

$$(4.2)$$

where $\tau_{-} << \tau_{+}$.

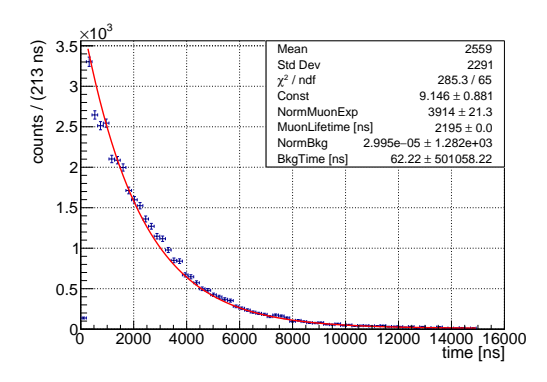
Since the distribution of muon decay times contributes only in the first range of values, to facilitate the fit of the final distribution, a two-step procedure was used. First of all, it performs a fitting operation on the data within the time range of 2000 to 15000 ns, employing a negative exponential model with a constant background. Subsequently, the obtained fit results serve as fixed parameters for a second fitting process conducted within the 200 to 16000 ns range. This second fit involves a combination of two exponentials, where one set of parameters is constrained based on the outcomes of the previous fit, while the other set remains free.

Another possible fit strategy could be adding a constraint in the ratio between the number of muons and antimuons. As reported in section 2.1, that ratio is equal to 1.25 for muons (antimuons) within the GeV energy range. Therefore, in principle it could be useful the following expression for the muon decay time distribution:

$$f(t) = c + N \left[0.555e^{-\frac{t}{\tau_{-}}} + 0.445e^{-\frac{t}{\tau_{+}}} \right]$$
 (4.3)

This second strategy yields two exponential with the same τ compatible with antimuon average lifetime, meaning that the fit algorithm is suppressing any extra contributions. Given this result, the following discussion focuses on the first proposed fit strategy.

On the left side of figure 4.3 it is reported the fit result, which suggests that the contribution of muons is negligible compared with the constant background, and this confirms the model chosen in the section 4.1.2. Moreover, on the right side there is a colormap plot of the same analysis taking into account the level of correlation between the background normalization and background τ . It can be seen that χ^2 minimum is obtained by suppressing the contribution of the exponential background, through either a very small average lifetime, or through a negligible normalization constant. This is an additional confirmation supporting the choice of neglecting the contribution of negative muons.



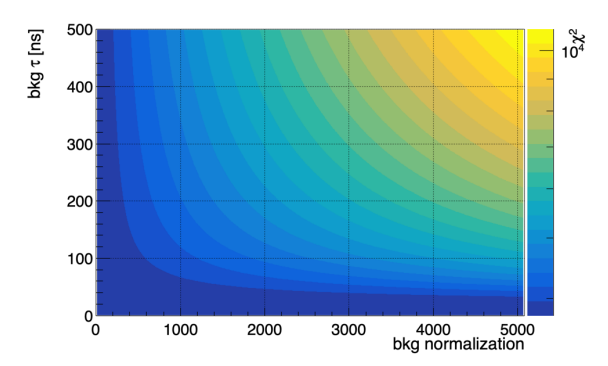


Figure 4.3: On the left. Fit results of the analysis with the function 4.2. On the right. χ^2 as a function of normalization and τ of the contribution of negative muons.

4.2 q Estimation

To determine the g-factor of the muon, we can conduct another round of data collection, similar to what was done for the lifetime measurement, but with the magnetic field activated. This will cause the muons that stop in copper to begin precessing around the magnetic field with an angular frequency determined by g.

The mathematical model employed has been previously elucidated in section 2.2 (see Eqs. 2.7 and 2.9). This enables us to consider both constant noise and the precession induced by \vec{B} . The formula utilized encompasses six parameters, rendering the fitting process rather intricate. Ideally, we would have preferred to incorporate the outcomes of section 4.1.2 where feasible, to diminish the parameters required. However, this was precluded due to the necessity of replacing certain SiPMs in the detectors, effectively bifurcating the two analyses: average lifetime and g estimation.

The data collection took place over a period of 100 days, where the SiPM and the solenoid were constantly in operation. The solenoid, in particular, heated up to approximately 45°C due to joule effect, subsequently elevating the temperature of the SiPMs housed within. These can either become more noisy due to high temperatures, which increase thermal noise, or due to other factors that have not been previously studied, like possible correlated noises from the power supply or any other electronic device involved.

Let's first see the noise study which was designed to identify any noise, and then proceed to perform the fit of the data collected.

4.2.1 Correlated Noise Analysis

From a theoretical perspective, the muon lifetimes recorded by the apparatus should follow a trend described by expression 2.9. In a real case, this expression needs to be modified to account for background noise, which may be due to electronic noise contributions or other types of radiation besides muons.

The subsequent analysis aims to assess the presence of correlated electronic noise and it is based on the assumption that this contribution results in an increase in the frequency of signal peaks. As a consequence of this phenomenon, the values returned by the apparatus will correspond to sequences of anomalous lifetimes, whose values are related to the frequency of electronic noise. To identify these sequences, consecutive events windows have been created and evaluated relative to a condition. Given a window, its probability can be defined as the joint probability of obtaining the set of events contained within it.

$$P_w = \prod_{i=1}^W P(t_i) \tag{4.4}$$

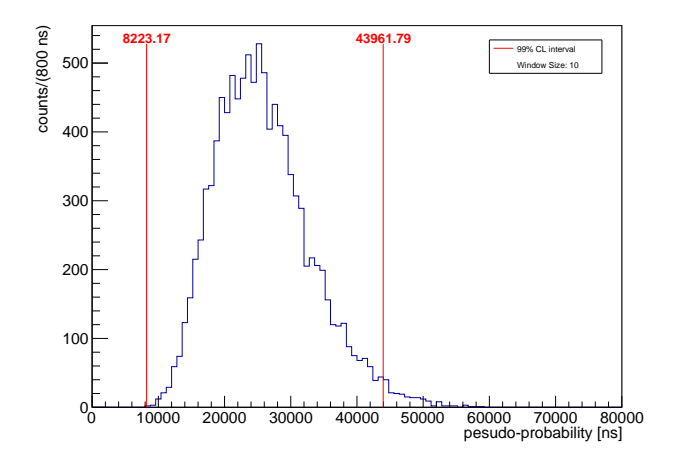


Figure 4.4: Window (width = 10) pseudo-probability distribution compared with 99% CL interval limits (red lines).

This quantity is calculated by multiplying the probabilities of individual events t, which can be defined as the product of the probability that no decay occurs between 0 and t and the probability that the decay occurs in a subsequent time interval. The first term is defined by the following expression:

$$P_0(0,t) = \left(1 - \frac{dt}{\tau}\right)^N \tag{4.5}$$

where N indicates the number of intervals dt composing the segment [0, t].

The probability of decay in a subsequent interval, given the properties of the Poisson distribution, is independent of the initial time t, so it is:

$$P_{\Delta t} = \frac{\Delta t}{\tau} = \frac{2\sigma}{\tau} \tag{4.6}$$

where $\Delta t = 2\sigma$ is assumed infinitesimal and it is defined as twice the temporal resolution of the apparatus (σ) .

In summary, the probability of a single event t is:

$$P(t) = \lim_{N \to \infty} \left[\left(1 - \frac{dt}{\tau} \right)^N \cdot \frac{2\sigma}{\tau} \right] = \frac{2\sigma}{\tau} e^{-t/\tau}$$
 (4.7)

Given these assumptions, a window consisting only of time events with smaller values than the muon lifetime has a higher probability than the average. On the other hand, larger than average time windows will have small probabilities. Thus, anomalous windows will have probabilities outside the reference range, that can be defined as the $1-\alpha$ confidence level interval of the window probability distribution.

In order to handle values that are not peaked to zero, this analysis is performed by taking the logarithm of eqn. 4.4:

$$\log(P_w) = \sum_{i=1}^{W} \log(P(t_i)) = W \log\left(\frac{2\sigma}{\tau}\right) - \frac{\sum_{i=1}^{W} t_i}{\tau}$$

$$\tag{4.8}$$

Given this expression, it is possible to define a pseudo-probability as

$$\tilde{P_w} = \sum_{i=1}^{W} t_i \tag{4.9}$$

Introducing this new quantity, it can be noticed that small (high) probabilities correspond to high (small) pseudo-probabilities, but it can still be used for the analysis.

A confidence interval can be calculated using Monte Carlo sampling from an exponential distribution, with the mean time obtained from the theoretical muon lifetime. By organizing consecutive events into subsets, one can calculate window pseudo-probabilities. These pseudo-probabilities can then be used to construct a distribution, from which confidence intervals can be determined by identifying the appropriate quantile values.

By utilizing the confidence interval limits, one can effectively assess whether the window pseudo-probabilities derived from real data fall within the specified range. Table 4.1 presents the analysis outcomes for various values of α . It is noteworthy that the right-hand side of the pseudo-probability distribution, which indicates an excess of long decay times, tends to have more outlier events than expected (see Fig. 4.4). This phenomenon could be attributed to several factors, including correlated noise. Consequently, it is worth limiting the analysis to the initial segment of the decay time distribution.

α	window size	expected outliers	left outliers	right outliers
0.05	5	270	30	563
0.05	10	270	20	770
0.05	20	269	15	1133
0.01	5	54	2	119
0.01	10	54	0	186
0.01	20	53	0	340

Table 4.1: Expected outliers compared with the outliers in pseudo-probability distribution tails as a function of α and window size.

4.2.2 q Analysis

For the estimation of g, the analysis ideally mirrors that used for the determination of the average lifetime, albeit with a different function that takes into account the precession of muons in the magnetic field. However, the situation in this specific case is somewhat more complex. As observed earlier, there appears to be some effect, possibly physical or noise-related, that causes a slight deviation in the histogram from the theoretically expected distribution. Given the inability to offer a definitive explanation for this observation and the inconclusive nature of the analysis using two exponentials as before (see Sec. 4.1.3), the function 2.7 was employed for the fit, but with some precautions.

$$N(\Delta t) = c + Ne^{-\Delta t/\tau} (1 + A\cos(\omega \Delta t + \phi))$$

Due to the limited number of events, decays occurring beyond 8000 ns cannot be incorporated into the fit. Furthermore, due to performance limitations of the Arietta, data for the initial 100 ns is unavailable as the system is unable to detect it. Therefore, the decision was made to fit within a range from 200 ns to 8000 ns, ensuring inclusion of data only within a reliable interval. In determining the approach to the fit, consideration must be given to the magnetic field's non-uniformity, which results in varying precession frequencies among muons. Although their values will be similar, they will not be identical, adding complexity to the fit. Moreover, as the function does not perfectly match the data, ensuring convergence of the minimization algorithm is not straightforward. The strategy employed is the following.

To aid convergence, the number of parameters is reduced by fixing τ . This value is derived from fitting the data without magnetic field in the range 200-8000 ns. It is important to note that this value roughly accounts for the observed anomalous trend together with the usual expected

counts from the exponential distribution. For this reason its meaning does not match exactly the muon average lifetime. It is possible to interpret τ as a parameter that deviates from the expected theoretical value due to some physical factors, such as anomalous SiPM performance and external noise contributions. Therefore its value ($\tau = 2.377 \pm 0.016~\mu s$) can be considered as a strong approximation of the overall physics that is involved.

Once a value for τ is obtained, a fit of the remaining parameters can be performed (see Fig. 4.5).

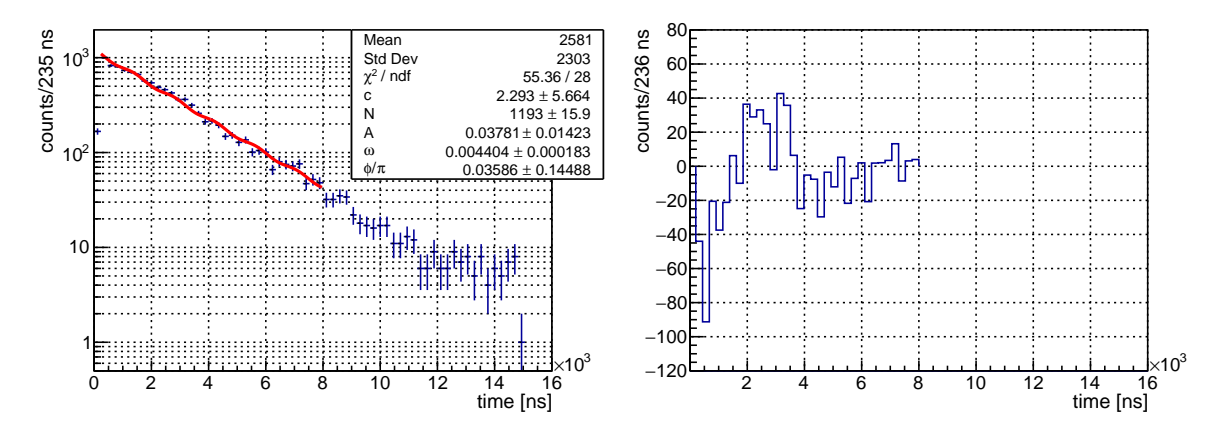


Figure 4.5: On the left. Fit of the data obtained with the magnetic field turned on. After fixing τ as discussed above it is possible to estimate the precession frequency of muons. On the right. Residuals of the fit printed only for the involved data, leaving zero counts elsewhere.

Before discussing the results, it is essential to recall that the primary focus lies on the oscillating function characterized by A, ω , and ϕ . Assessing the quality of the findings involves referring to values reported in the literature from analogous experiments [1].

The results of the fit appear to be consistent with what has already been observed. Unfortunately, not having carried out a simulation of the experimental setup used, it is difficult to understand whether the values obtained are exactly those expected. The outcome is influenced by a combination of underlying physics and the geometric characteristics of the experiment. Factors like non-uniform quantities such as magnetic field distribution and SiPM behavior over time contribute to the challenge of establishing a reliable theoretical expectation. Nonetheless, the obtained values can be considered satisfactory, as they appear to be within the expected order of magnitude and comparable to those reported in the literature.

After determining the value of ω , it becomes feasible to derive an estimate for g using the formula referenced in 4.10. For this calculation, the error was computed by considering only the errors associated with \vec{B} and ω , as the remaining involved quantities are estimated with great accuracy.

$$g = 2\frac{m_{\mu}\omega}{|\vec{B}|e} \qquad \sigma_g = g\sqrt{\left(\frac{\sigma_{\omega}}{\omega}\right)^2 + \left(\frac{\sigma_{|\vec{B}|}}{|\vec{B}|}\right)^2}$$
(4.10)

The final result is:

$$g = 1.85 \pm 0.09 \tag{4.11}$$

Chapter 5

Conclusions

This report outlines a proposed experimental setup for measuring the muon magnetic moment. Since muon production and decay hexibit maximal parity violation, the positioning of scintillator layers is critical, aiming to capture the muon lifetime by detecting the time difference between a muon absorbed by a copper layer and the subsequent emission of a positron due to muon decay in the upper region.

A crucial aspect is the definition of a trigger-veto logic capable of distinguishing between noise and genuine events. The goal is to configure a system with an exceedingly low rate of false positive events (background noise). Therefore, a thorough investigation into the performance of scintillators coupled with SiPMs is necessary to assess parameters such as gain, dark count rate, and signal distribution. However, the presence of significant electronic noise complicates the accurate estimation of these parameters. The same consideration involved the signal distribution, which presented a peak around 0 mV, meaning that the trigger system accepted a false positive signal.

With a comprehensive understanding of SiPM properties, it becomes feasible to select a threshold that balances a minimal false positive rate with high efficiency. To mitigate background contributions, the trigger-veto logic employs a redundant system to minimize random coincidences. Adopting a higher threshold enhances the discrimination between genuine events and false positives, albeit at the expense of system efficiency, estimated to be between 75% and 80%. Consequently, an extended data collection period of 100 days becomes necessary. On the other hand the rate of muon accidentals is acceptable for the execution of the measurements. Their contribution is taken into account in the offline analysis by supposing a flat background in the decay spectra. Furthermore, a systematic error arises from the magnetic field's inhomogeneity, approximately at 2%. This factor introduces additional uncertainties into the measurements.

First, the lifetime distribution of muons in the absence of magnetic field was analyzed to measure τ_{μ} . The results are compatible with theory only under certain conditions: it is necessary to limit the fitting interval between 2 and 15 μs because of the presence of an anomalous contribution at short times. This is confirmed by a fit within disjoint intervals of the entire time interval, since the first region (before 2500 ns) returns an unexpected τ_{μ} . Therefore, the exclusion of this region allows any extra contribution to the muon lifetime distribution to be neglected.

Another analysis of this distribution reveals that the apparatus is not sensitive enough to quantify the influence of negative muon decays, which are captured by nuclei, and this limits the accuracy of the measurements. Taking into account all these contributions, this analysis yields

$$\tau_{\mu} = 2.195 \pm 0.024 \; \mu s$$

After determining the average lifetime of the muon, the subsequent task involves estimating g, which serves as the primary objective of the experiment. This parameter entails a fitting procedure that encompasses six parameters. The fitting process is intricate due to the multitude of parameters and the presence of substantial noise components, alongside the physical limitations

of the experiment.

To address these challenges, a noise detection analysis was devised to identify noise based on available data. This method relies on detecting "unlikely clusters of subsequent events" that deviate from the expected theoretical distribution, allowing the identification of anomalies at higher or lower times and mitigate some of the noise. However, this approach did not prove effective enough to clean and incorporate data beyond $\Delta t > 8 \ \mu s$.

Given the high ratio of noise counts to signal counts $\frac{\text{noise counts}}{\text{signal counts}}$ at higher Δt values, observations beyond 8 μs must be discounted as they are indistinguishable from noise. Additionally, the non-uniformity of the magnetic field introduced by the experimental setup results in composite oscillations composed of sinusoidal functions, each exhibiting similar but not identical angular frequencies (ω).

In conclusion, the value obtained is:

$$g = 1.85 \pm 0.09$$

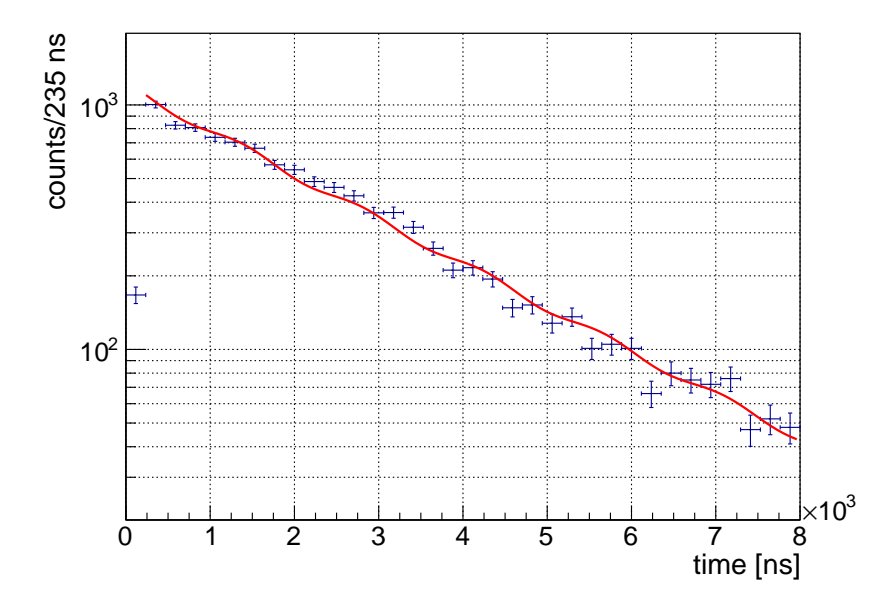


Figure 5.1: Fit performed on the data to get the frequency of the oscillation. In this zoom version of plot in figure 4.5 the oscillation is clearly visible.

Within its margin of error, the result is largely consistent with the theoretical value. Unfortunately, the precision of the obtained value is approximately 5%, a satisfactory outcome achieved with considerable effort due to noise and limited data availability. Throughout the discussion, the encountered issues were addressed, and various potential solutions were proposed. In particular, prioritizing the unreliability of SiPMs is considered most urgent. At times, these devices malfunctioned temporarily before resuming normal operation. However, in some instances, they failed entirely, necessitating replacement and invalidating many previous considerations.

Bibliography

- [1] C. Amsler. The determination of the muon magnetic moment from cosmic rays. *American Journal of Physics*, 42(12), 1974.
- [2] D. Bosnar et al. A simple setup for the determination of the cosmic muon magnetic moment. American Journal of Physics, 90(8), August 2022.
- [3] E. Bulyak and N. Shul'ga. Landau distribution of ionization losses: history, importance, extensions, 2022.
- [4] R L. Garwin et al. Observations of the failure of conservation of parity and charge conjugation in meson decays: the magnetic moment of the free muon. *Phys. Rev.*, 105, Feb 1957.
- [5] A. Ghassemi et al. A technical guide to silicon photomultipliers (MPPC). Hamamatsu, 2017.
- [6] L.D. Landau. On the energy loss of fast particles by ionization. J. Phys., 8(4), 1944.
- [7] L. Liu and P. Solis. The speed and lifetime of cosmic ray muons. *Physics Department, Massachusetts Institute of Technology, Cambridge, MA*, 2139, 2007.
- [8] W. Newhauser and R. Zhang. The physics of proton therapy. *Physics in medicine and biology*, 60, 03 2015.
- [9] B. B. Rossi. High-energy particles. Prentice-Hall physics series. Prentice-Hall, New York, NY, 1952.
- [10] Z.K. Silagadze. A new algorithm for automatic photopeak searches. arXiv preprint hep-ex/9506013, 1995.
- [11] R. L. Workman et al. Review of Particle Physics. PTEP, 2022, 2023.
- [12] P. A. Zyla et al. Review of Particle Physics. *Progress of Theoretical and Experimental Physics*, 2020(8), 08 2020.